Research Article | Vol. 9, No. 7 | 1 Jul 2018 | BIOMEDICAL OPTICS EXPRESS 3399
Biomedical Optics EXPRESS

Near-simultaneous quantification of glucose uptake, mitochondrial membrane potential, and vascular parameters in murine flank tumors using quantitative diffuse reflectance and fluorescence spectroscopy

CAIGANG ZHU,[1] HANNAH L. MARTIN,[1] BRIAN T. CROUCH,[1] AMY F. MARTINEZ,[2] MARTIN LI,[1] GREGORY M. PALMER,[3] MARK W. DEWHIRST,[3] AND NIMMI RAMANUJAM[1,*]

[1]*Department of Biomedical Engineering, Duke University, Durham, NC 27708, USA*
[2]*Currently with Office of Research, Vanderbilt University Medical Center, Nashville, TN 37232, USA*
[3]*Department of Radiation Oncology, Duke University, Durham, NC 27710, USA*
**nimmi@duke.edu*

Abstract: The shifting metabolic landscape of aggressive tumors, with fluctuating oxygenation conditions and temporal changes in glycolysis and mitochondrial metabolism, is a critical phenomenon to study in order to understand negative treatment outcomes. Recently, we have demonstrated near-simultaneous optical imaging of mitochondrial membrane potential (MMP) and glucose uptake in non-tumor window chambers, using the fluorescent probes tetramethylrhodamine ethyl ester (TMRE) and 2-N-(7-nitrobenz-2-oxa-1,3-diazol-4-yl)amino)-2-deoxyglucose (2-NBDG). Here, we demonstrate a complementary technique to perform near-simultaneous *in vivo* optical spectroscopy of tissue vascular parameters, glucose uptake, and MMP in a solid tumor model that is most often used for therapeutic studies. Our study demonstrates the potential of optical spectroscopy as an effective tool to quantify the vascular and metabolic characteristics of a tumor, which is an important step towards understanding the mechanisms underlying cancer progression, metastasis, and resistance to therapies.

OCIS codes: (170.6280) Spectroscopy, fluorescence and luminescence; (170.6510) Spectroscopy, tissue diagnostics; (170.4580) Optical diagnostics for medicine; (170.6935) Tissue characterization.

References and links

1. O. Warburg, K. Posener, and E. Negelein, "On the metabolism of carcinoma cells," Biochem. Z. **152**, 309–344 (1924).
2. R. V. Simões, I. S. Serganova, N. Kruchevsky, A. Leftin, A. A. Shestov, H. T. Thaler, G. Sukenick, J. W. Locasale, R. G. Blasberg, J. A. Koutcher, and E. Ackerstaff, "Metabolic plasticity of metastatic breast cancer cells: adaptation to changes in the microenvironment," Neoplasia **17**(8), 671–684 (2015).
3. A. Viale, D. Corti, and G. F. Draetta, "Tumors and mitochondrial respiration: a neglected connection," Cancer Res. **75**(18), 3685–3687 (2015).
4. T. Epstein, L. Xu, R. J. Gillies, and R. A. Gatenby, "Separation of metabolic supply and demand: aerobic glycolysis as a normal physiological response to fluctuating energetic demands in the membrane," Cancer Metab. **2**(1), 7 (2014).
5. C. Jose, N. Bellance, and R. Rossignol, "Choosing between glycolysis and oxidative phosphorylation: A tumor's dilemma?" Biochim. Biophys. Acta **1807**(6), 552–561 (2011).
6. A. L. Maas, S. L. Carter, E. P. Wileyto, J. Miller, M. Yuan, G. Yu, A. C. Durham, and T. M. Busch, "Tumor vascular microenvironment determines responsiveness to photodynamic therapy," Cancer Res. **72**(8), 2079–2088 (2012).
7. R. A. Gatenby and R. J. Gillies, "Why do cancers have high aerobic glycolysis?" Nat. Rev. Cancer **4**(11), 891–899 (2004).
8. S. P. M. Crouch, R. Kozlowski, K. J. Slater, and J. Fletcher, "The use of ATP bioluminescence as a measure of cell proliferation and cytotoxicity," J. Immunol. Methods **160**(1), 81–88 (1993).

#328946 https://doi.org/10.1364/BOE.9.003399
Journal © 2018 Received 20 Apr 2018; revised 14 Jun 2018; accepted 18 Jun 2018; published 27 Jun 2018

Biomedical Optics EXPRESS

9. R. C. Scaduto, Jr. and L. W. Grotyohann, "Measurement of mitochondrial membrane potential using fluorescent rhodamine derivatives," Biophys. J. **76**(1), 469–477 (1999).
10. A. V. Kuznetsov, V. Veksler, F. N. Gellerich, V. Saks, R. Margreiter, and W. S. Kunz, "Analysis of mitochondrial function in situ in permeabilized muscle fibers, tissues and cells," Nat. Protoc. **3**(6), 965–976 (2008).
11. V. Chen, R. E. Staub, S. Fong, M. Tagliaferri, I. Cohen, and E. Shtivelman, "Bezielle selectively targets mitochondria of cancer cells to inhibit glycolysis and OXPHOS," PLoS One **7**(2), e30300 (2012).
12. S. Akakura, E. Ostrakhovitch, R. Sanokawa-Akakura, and S. Tabibzadeh, "Cancer cells recovering from damage exhibit mitochondrial restructuring and increased aerobic glycolysis," Biochem. Biophys. Res. Commun. **448**(4), 461–466 (2014).
13. S. Y. Wang, Y. H. Wei, D. B. Shieh, L. L. Lin, S. P. Cheng, P. W. Wang, and J. H. Chuang, "2-Deoxy-d-glucose can complement doxorubicin and sorafenib to suppress the growth of papillary thyroid carcinoma cells," PLoS One **10**(7), e0130959 (2015).
14. "*http://www.seahorsebio.com/learning/publications.php*" (2018), retrieved March 30, 2018.
15. G. Cheng, J. Zielonka, D. McAllister, S. Tsai, M. B. Dwinell, and B. Kalyanaraman, "Profiling and targeting of cellular bioenergetics: inhibition of pancreatic cancer cell proliferation," Br. J. Cancer **111**(1), 85–93 (2014).
16. R. V. Simões, I. S. Serganova, N. Kruchevsky, A. Leftin, A. A. Shestov, H. T. Thaler, G. Sukenick, J. W. Locasale, R. G. Blasberg, J. A. Koutcher, and E. Ackerstaff, "Metabolic plasticity of metastatic breast cancer cells: adaptation to changes in the microenvironment," Neoplasia **17**(8), 671–684 (2015).
17. L. Shen, J. M. O'Shea, M. R. Kaadige, S. Cunha, B. R. Wilde, A. L. Cohen, A. L. Welm, and D. E. Ayer, "Metabolic reprogramming in triple-negative breast cancer through MYC suppression of TXNIP," Proc. Natl. Acad. Sci. U.S.A. **112**(17), 5425–5430 (2015).
18. H. Wu, A. D. Southam, A. Hines, and M. R. Viant, "High-throughput tissue extraction protocol for NMR- and MS-based metabolomics," Anal. Biochem. **372**(2), 204–212 (2008).
19. E. J. Want, P. Masson, F. Michopoulos, I. D. Wilson, G. Theodoridis, R. S. Plumb, J. Shockcor, N. Loftus, E. Holmes, and J. K. Nicholson, "Global metabolic profiling of animal and human tissues via UPLC-MS," Nat. Protoc. **8**(1), 17–32 (2012).
20. M. Mehrmohamadi, S. H. Jeong, and J. W. Locasale, "Molecular features that predict the response to antimetabolite chemotherapies," Cancer Metab. **5**(1), 8 (2017).
21. Z. Dai, A. A. Shestov, L. Lai, and J. W. Locasale, "A flux balance of glucose metabolism clarifies the requirements of the Warburg effect," Biophys. J. **111**(5), 1088–1100 (2016).
22. X. Lu, B. Bennet, E. Mu, J. Rabinowitz, and Y. Kang, "Metabolomic changes accompanying transformation and acquisition of metastatic potential in a syngeneic mouse mammary tumor model," J. Biol. Chem. **285**(13), 9317–9321 (2010).
23. A. Chokkathukalam, D. H. Kim, M. P. Barrett, R. Breitling, and D. J. Creek, "Stable isotope-labeling studies in metabolomics: new insights into structure and dynamics of metabolic networks," Bioanalysis **6**(4), 511–524 (2014).
24. G. J. Kelloff, J. M. Hoffman, B. Johnson, H. I. Scher, B. A. Siegel, E. Y. Cheng, B. D. Cheson, J. O'shaughnessy, K. Z. Guyton, D. A. Mankoff, L. Shankar, S. M. Larson, C. C. Sigman, R. L. Schilsky, and D. C. Sullivan, "Progress and promise of FDG-PET imaging for cancer patient management and oncologic drug development," Clin. Cancer Res. **11**(8), 2785–2808 (2005).
25. J. F. Eary and D. A. Mankoff, "Tumor metabolic rates in sarcoma using FDG PET," J. Nucl. Med. **39**(2), 250–254 (1998).
26. B. Huang, P. L. Khong, D. L. W. Kwong, B. Hung, C. S. Wong, and C. Y. O. Wong, "Dynamic PET-CT studies for characterizing nasopharyngeal carcinoma metabolism: comparison of analytical methods," Nucl. Med. Commun. **33**(2), 191–197 (2012).
27. H. Qiao, J. Li, Y. Chen, D. Wang, J. Han, M. Mei, and D. Li, "A study of the metabolism of transplanted tumor in the lung by micro PET/CT in mice," Med. Eng. Phys. **36**(3), 294–299 (2014).
28. K. Tanimoto, K. Yoshikawa, T. Obata, H. Ikehira, T. Shiraishi, K. Watanabe, T. Saga, J. Mizoe, T. Kamada, A. Kato, and M. Miyazaki, "Role of glucose metabolism and cellularity for tumor malignancy evaluation using FDG-PET/CT and MRI," Nucl. Med. Commun. **31**(6), 604–609 (2010).
29. A. Welch, M. Mingarelli, G. Riedel, and B. Platt, "Mapping changes in mouse brain metabolism with PET/CT," J. Nucl. Med. **54**(11), 1946–1953 (2013).
30. H. Cho, E. Ackerstaff, S. Carlin, M. E. Lupu, Y. Wang, A. Rizwan, J. O'Donoghue, C. C. Ling, J. L. Humm, P. B. Zanzonico, and J. A. Koutcher, "Noninvasive multimodality imaging of the tumor microenvironment: registered dynamic magnetic resonance imaging and positron emission tomography studies of a preclinical tumor model of tumor hypoxia," Neoplasia **11**(3), 247–259 (2009).
31. K. Glunde and Z. M. Bhujwalla, "Metabolic tumor imaging using magnetic resonance spectroscopy," Semin. Oncol. **38**(1), 26–41 (2011).
32. R. J. Gillies and D. L. Morse, "In vivo magnetic resonance spectroscopy in cancer," Annu. Rev. Biomed. Eng. **7**(1), 287–326 (2005).
33. M. L. James and S. S. Gambhir, "A molecular imaging primer: modalities, imaging agents, and applications," Physiol. Rev. **92**(2), 897–965 (2012).

Biomedical Optics EXPRESS

34. R. Alonzi, A. R. Padhani, N. J. Taylor, D. J. Collins, J. A. D'Arcy, J. J. Stirling, M. I. Saunders, and P. J. Hoskin, "Antivascular effects of neoadjuvant androgen deprivation for prostate cancer: an *in vivo* human study using susceptibility and relaxivity dynamic MRI," Int. J. Radiat. Oncol. Biol. Phys. **80**(3), 721–727 (2011).
35. N. J. Taylor, H. Baddeley, K. A. Goodchild, M. E. B. Powell, M. Thoumine, L. A. Culver, J. J. Stirling, M. I. Saunders, P. J. Hoskin, H. Phillips, A. R. Padhani, and J. R. Griffiths, "BOLD MRI of human tumor oxygenation during carbogen breathing," J. Magn. Reson. Imaging **14**(2), 156–163 (2001).
36. J. P. B. O'Connor, A. Jackson, G. J. M. Parker, and G. C. Jayson, "DCE-MRI biomarkers in the clinical evaluation of antiangiogenic and vascular disrupting agents," Br. J. Cancer **96**(2), 189–195 (2007).
37. M. Fuss, F. Wenz, M. Essig, M. Muenter, J. Debus, T. S. Herman, and M. Wannenmacher, "Tumor angiogenesis of low-grade astrocytomas measured by dynamic susceptibility contrast-enhanced MRI (DSC-MRI) is predictive of local tumor control after radiation therapy," Int. J. Radiat. Oncol. Biol. Phys. **51**(2), 478–482 (2001).
38. M. Solomon, Y. Liu, M. Y. Berezin, and S. Achilefu, "Optical imaging in cancer research: basic principles, tumor detection, and therapeutic monitoring," Med. Princ. Pract. **20**(5), 397–415 (2011).
39. M. N. Loja, Z. Luo, D. Greg Farwell, Q. C. Luu, P. J. Donald, D. Amott, A. Q. Truong, R. F. Gandour-Edwards, and N. Nitin, "Optical molecular imaging detects changes in extracellular pH with the development of head and neck cancer," Int. J. Cancer **132**(7), 1613–1623 (2013).
40. A. J. Walsh, R. S. Cook, H. C. Manning, D. J. Hicks, A. Lafontant, C. L. Arteaga, and M. C. Skala, "Optical metabolic imaging identifies glycolytic levels, subtypes, and early-treatment response in breast cancer," Cancer Res. **73**(20), 6164–6174 (2013).
41. X. Liu, Z. Ser, and J. W. Locasale, "Development and quantitative evaluation of a high-resolution metabolomics technology," Anal. Chem. **86**(4), 2175–2184 (2014).
42. A. T. Shah, M. Demory Beckler, A. J. Walsh, W. P. Jones, P. R. Pohlmann, and M. C. Skala, "Optical metabolic imaging of treatment response in human head and neck squamous cell carcinoma," PLoS One **9**(3), e90746 (2014).
43. A. J. Walsh, R. S. Cook, M. E. Sanders, L. Aurisicchio, G. Ciliberto, C. L. Arteaga, and M. C. Skala, "Quantitative optical imaging of primary tumor organoid metabolism predicts drug response in breast cancer," Cancer Res. **74**(18), 5184–5194 (2014).
44. N. Rajaram, A. F. Reesor, C. S. Mulvey, A. E. Frees, and N. Ramanujam, "Non-invasive, simultaneous quantification of vascular oxygenation and glucose uptake in tissue," PLoS One **10**(1), e0117132 (2015).
45. M. C. Skala, K. M. Riching, A. Gendron-Fitzpatrick, J. Eickhoff, K. W. Eliceiri, J. G. White, and N. Ramanujam, "In vivo multiphoton microscopy of NADH and FAD redox states, fluorescence lifetimes, and cellular morphology in precancerous epithelia," Proc. Natl. Acad. Sci. U.S.A. **104**(49), 19494–19499 (2007).
46. J. Hou, H. J. Wright, N. Chan, R. Tran, O. V. Razorenova, E. O. Potma, and B. J. Tromberg, "Correlating two-photon excited fluorescence imaging of breast cancer cellular redox state with seahorse flux analysis of normalized cellular oxygen consumption," J. Biomed. Opt. **21**(6), 060503 (2016).
47. N. Ramanujam, "Fluorescence spectroscopy of neoplastic and non-neoplastic tissues," Neoplasia **2**(1-2), 89–117 (2000).
48. N. Rajaram, A. E. Frees, A. N. Fontanella, J. Zhong, K. Hansen, M. W. Dewhirst, and N. Ramanujam, "Delivery rate affects uptake of a fluorescent glucose analog in murine metastatic breast cancer," PLoS One **8**(10), e76524 (2013).
49. A. E. Frees, N. Rajaram, S. S. McCachren 3rd, A. N. Fontanella, M. W. Dewhirst, and N. Ramanujam, "Delivery-corrected imaging of fluorescently-labeled glucose reveals distinct metabolic phenotypes in murine breast cancer," PLoS One **9**(12), e115529 (2014).
50. C. G. Zhu, A. F. Martinez, H. L. Martin, M. Li, B. T. Crouch, D. A. Carlson, T. A. J. Haystead, and N. Ramanujam, "Near-simultaneous intravital microscopy of glucose uptake and mitochondrial membrane potential, key endpoints that reflect major metabolic axes in cancer," Sci. Rep. **7**, 13772 (2017).
51. A. F. Martinez, S. S. McCachren 3rd, M. Lee, H. A. Murphy, C. Zhu, B. T. Crouch, H. L. Martin, A. Erkanli, N. Rajaram, K. A. Ashcraft, A. N. Fontanella, M. W. Dewhirst, and N. Ramanujam, "Metaboloptics: Visualization of the tumor functional landscape via metabolic and vascular imaging," Sci. Rep. **8**(1), 4171 (2018).
52. U. E. Martinez-Outschoorn, M. Peiris-Pagés, R. G. Pestell, F. Sotgia, and M. P. Lisanti, "Cancer metabolism: a therapeutic perspective," Nat. Rev. Clin. Oncol. **14**(2), 113 (2017).
53. J. E. Bender, K. Vishwanath, L. K. Moore, J. Q. Brown, V. Chang, G. M. Palmer, and N. Ramanujam, "A robust Monte Carlo model for the extraction of biological absorption and scattering in vivo," IEEE Trans. Biomed. Eng. **56**(4), 960–968 (2009).
54. G. M. Palmer, R. J. Boruta, B. L. Viglianti, L. Lan, I. Spasojevic, and M. W. Dewhirst, "Non-invasive monitoring of intra-tumor drug concentration and therapeutic response using optical spectroscopy," J. Control. Release **142**(3), 457–464 (2010).
55. G. M. Palmer and N. Ramanujam, "Monte-Carlo-based model for the extraction of intrinsic fluorescence from turbid media," J. Biomed. Opt. **13**(2), 024017 (2008).
56. C. B. Liu, N. Rajaram, K. Vishwanath, T. Jiang, G. M. Palmer, and N. Ramanujam, "Experimental validation of an inverse fluorescence Monte Carlo model to extract concentrations of metabolically relevant fluorophores from turbid phantoms and a murine tumor model," J. Biomed. Opt. **17**, 078003 (2012).
57. "*https://omlc.org/spectra/hemoglobin/"*, retrieved 2018.
58. Q. Fu and W. Sun, "Mie theory for light scattering by a spherical particle in an absorbing medium," Appl. Opt. **40**(9), 1354–1361 (2001).

Biomedical Optics EXPRESS

59. C. Constantinides, R. Mean, and B. J. Janssen, "Effects of isoflurane anesthesia on the cardiovascular function of the C57BL/6 mouse," ILAR J. **52**(3), e21–e31 (2011).
60. G. M. Palmer, A. N. Fontanella, S. Shan, G. Hanna, G. Zhang, C. L. Fraser, and M. W. Dewhirst, "*In vivo* optical molecular imaging and analysis in mice using dorsal window chamber models applied to hypoxia, vasculature and fluorescent reporters," Nat. Protoc. **6**(9), 1355–1366 (2011).
61. J. Kahn, P. J. Tofilon, and K. Camphausen, "Preclinical models in radiation oncology," Radiat. Oncol. **7**(1), 223 (2012).
62. I. Serganova, A. Rizwan, X. Ni, S. B. Thakur, J. Vider, J. Russell, R. Blasberg, and J. A. Koutcher, "Metabolic imaging: a link between lactate dehydrogenase a, lactate, and tumor phenotype," Clin. Cancer Res. **17**(19), 6250–6261 (2011).
63. X. Lu, B. Bennet, E. Mu, J. Rabinowitz, and Y. Kang, "Metabolomic changes accompanying transformation and acquisition of metastatic potential in a syngeneic mouse mammary tumor model," J. Biol. Chem. **285**(13), 9317–9321 (2010).
64. I. Serganova, A. Rizwan, X. Ni, S. B. Thakur, J. Vider, J. Russell, R. Blasberg, and J. A. Koutcher, "Metabolic imaging: a link between lactate dehydrogenase A, lactate, and tumor phenotype," Clin. Cancer Res. **17**(19), 6250–6261 (2011).
65. U. E. Martinez-Outschoorn, M. Prisco, A. Ertel, A. Tsirigos, Z. Lin, S. Pavlides, C. Wang, N. Flomenberg, E. S. Knudsen, A. Howell, R. G. Pestell, F. Sotgia, and M. P. Lisanti, "Ketones and lactate increase cancer cell "stemness," driving recurrence, metastasis and poor clinical outcome in breast cancer: achieving personalized medicine via Metabolo-Genomics," Cell Cycle **10**(8), 1271–1286 (2011).
66. P. E. Porporato, V. L. Payen, J. Pérez-Escuredo, C. J. De Saedeleer, P. Danhier, T. Copetti, S. Dhup, M. Tardy, T. Vazeille, C. Bouzin, O. Feron, C. Michiels, B. Gallez, and P. Sonveaux, "A mitochondrial switch promotes tumor metastasis," Cell Reports **8**(3), 754–766 (2014).
67. P. Li, D. Zhang, L. Shen, K. Dong, M. Wu, Z. Ou, and D. Shi, "Redox homeostasis protects mitochondria through accelerating ROS conversion to enhance hypoxia resistance in cancer cells," Sci. Rep. **6**(1), 22831 (2016).
68. K. Vishwanath, H. Yuan, W. T. Barry, M. W. Dewhirst, and N. Ramanujam, "Using optical spectroscopy to longitudinally monitor physiological changes within solid tumors," Neoplasia **11**(9), 889–900 (2009).
69. C. P. Sabino, A. M. Deana, T. M. Yoshimura, D. F. da Silva, C. M. França, M. R. Hamblin, and M. S. Ribeiro, "The optical properties of mouse skin in the visible and near infrared spectral regions," J. Photochem. Photobiol. B **160**, 72–78 (2016).
70. J. Folkman, "Angiogenesis in cancer, vascular, rheumatoid and other disease," Nat. Med. **1**(1), 27–30 (1995).
71. B. R. Zetter, "Angiogenesis and tumor metastasis," Annu. Rev. Med. **49**, 407–424 (1998).
72. C. Y. Li, S. Shan, Q. Huang, R. D. Braun, J. Lanzen, K. Hu, P. Lin, and M. W. Dewhirst, "Initial stages of tumor cell-induced angiogenesis: evaluation via skin window chambers in rodent models," J. Natl. Cancer Inst. **92**(2), 143–147 (2000).
73. D. Zhao, Y. Tu, L. Wan, L. Bu, T. Huang, X. Sun, K. Wang, and B. Shen, "*In vivo* monitoring of angiogenesis inhibition via down-regulation of mir-21 in a VEGFR2-luc murine breast cancer model using bioluminescent imaging," PLoS One **8**(8), e71472 (2013).
74. P. Vaupel, A. Mayer, and M. Höckel, "Tumor hypoxia and malignant progression," Methods Enzymol. **381**, 335–354 (2004).
75. I. J. Hoogsteen, H. A. Marres, A. J. van der Kogel, and J. H. A. M. Kaanders, "The hypoxic tumour microenvironment, patient selection and hypoxia-modifying treatments," Clin. Oncol. (R Coll Radiol) **19**(6), 385–396 (2007).
76. A. Carcereri de Prati, E. Butturini, A. Rigo, E. Oppici, M. Rossin, D. Boriero, and S. Mariotto, "Metastatic breast cancer cells enter into dormant state and express cancer stem cells phenotype under chronic hypoxia," J. Cell. Biochem. **118**(10), 3237–3248 (2017).
77. P. E. Porporato, S. Dhup, R. K. Dadhich, T. Copetti, and P. Sonveaux, "Anticancer targets in the glycolytic metabolism of tumors: a comprehensive review," Front. Pharmacol. **2**, 49 (2011).
78. G. Fluegen, A. Avivar-Valderas, Y. Wang, M. R. Padgen, J. K. Williams, A. R. Nobre, V. Calvo, J. F. Cheung, J. J. Bravo-Cordero, D. Entenberg, J. Castracane, V. Verkhusha, P. J. Keely, J. Condeelis, and J. A. Aguirre-Ghiso, "Phenotypic heterogeneity of disseminated tumour cells is preset by primary tumour hypoxic microenvironments," Nat. Cell Biol. **19**(2), 120–132 (2017).
79. M. W. Dewhirst, Y. Cao, and B. Moeller, "Cycling hypoxia and free radicals regulate angiogenesis and radiotherapy response," Nat. Rev. Cancer **8**(6), 425–437 (2008).

1. Introduction

Interest in tumor metabolism and vasculature continues to grow in the field of cancer research. Beyond the extensively studied "Warburg effect" [1], which reflects a tumor's propensity for aerobic glycolysis, mitochondria have recently gained recognition for their distinct contribution to tumor oxidative metabolism. In fact, some tumors can switch their primary metabolic mode between glycolysis and oxidative phosphorylation to meet increased energy demands required for proliferation and metastasis [2–4], as well as adapt to stressors

Biomedical Optics EXPRESS

including chemo and molecular therapies [5]. The vascular microenvironment is another critical enabler of tumor survival and recurrence [6] since it will influence tumor metabolism. Specifically, vascular oxygen saturation (SO_2) and hemoglobin concentration ([Hb]) within the tumor microenvironment influences metabolism by affecting metabolic substrate availability; conversely, metabolic needs affect vascular parameters by dictating substrate demand [7]. Taken together, glycolysis, mitochondrial oxidative phosphorylation, and vascular parameters all play a key role in understanding how the metabolic characteristics of tumors impact therapeutic outcome, and the ability to monitor all of them simultaneously can play an important role in cancer pharmacology research.

A common tool for assessing glycolysis and oxidative phosphorylation is the ubiquitous Seahorse Assay, which treats cells *in vitro* with chemical perturbations to measure two functional endpoints: oxygen consumption rate (OCR) and extracellular acidification rate (ECAR) [8–13]. The Seahorse instrument is widely used for biomedical research as evidenced by over 500 journal articles in 2017 alone [14]. In the cancer research field, the Seahorse Assay has been frequently used to investigate metabolic characteristics associated with cell proliferation and apoptosis [15], response to therapeutic stress [16], and metabolic reprogramming in metastatic breast cancer cells [17], to name just a few examples. However, a major limitation of the Seahorse Assay is its utility is restricted to *in vitro* cell samples, preventing both the investigation of metabolism *in vivo* and the effect of the vasculature within the tumor microenvironment on tumor metabolism. Metabolomics, the gold standard for measurement of metabolites, can quickly screen a large number of molecules and map metabolic networks [18, 19]. Metabolomics has been frequently used to evaluate the effect of chemotherapy on metabolite levels [20], understand how the "Warburg effect" promotes tumor survival [21], and identify unique metabolites in metastatic tumors [22]. However, metabolomics is mainly used for *ex vivo* tissue samples and only provides a snapshot of the tissue's metabolic state. By using ^{13}C labeled glucose or other metabolites, it is possible to acquire metabolic fluxes [23]. However, this requires highly sophisticated technology and software for such analyses. There are several techniques currently available for *in vivo* metabolic imaging including Positron Emission Tomography (PET) and magnetic resonance imaging (MRI). PET is able to quantify glucose uptake using ^{18}F-FDG [24–29]. PET can also image hypoxia using other radio-labeled probes (e.g.^{18}FFMISO) [30], however, both glucose uptake and hypoxia cannot be measured simultaneously. Magnetic resonance spectral imaging (MR(S)I) can report on mitochondrial metabolism and glycolysis using special tracers such as ^{31}P or hyperpolarized ^{13}C labeled compounds [31, 32]. Additionally, vascular imaging can be accomplished with a range of magnetic resonance imaging (MRI) techniques [33, 34], including blood oxygen level dependent (BOLD) MRI [33, 35], dynamic contrast-enhanced (DCE) MRI [30, 36], and dynamic susceptibility contrast (DSC) MRI [37]. While each of these tools enable organ-level imaging, the endpoints provide relative measurements and the endpoints cannot be imaged simultaneously. Ultimately, however, there are tradeoffs between the MRI, PET and optical spectroscopy and we believe that the latter will fit well within the suite of technologies available for metabolic and vascular assessment of tumors.

Optical spectroscopy and imaging can leverage endogenous contrast or be coupled with appropriate indicators to provide quantitative endpoints related tumor metabolism and its associated vasculature *in vivo* [38–44]. Two endogenous fluorophores in tissue, reduced nicotinamide adenine dinucleotide (NADH) and flavin adenine dinucleotide (FAD) [43, 45] provide insights into the reduction-oxidation state in the electron transport chain, as NADH fluorescence is increased in tumors reliant on glycolysis, whereas increased FAD fluorescence corresponds to more oxidative tumors [46]. It should be noted that the ratio of NADH and FAD does not directly report on glucose uptake nor mitochondrial activity given that cytosolic NAD(P)H also contributes to endogenous fluorescence that is similar to that of NADH, and FAD fluorescence is relatively weak [47]. Our group has developed a novel technique to quantify glucose uptake and mitochondrial metabolism using the fluorescent

Biomedical Optics EXPRESS

glucose analog 2-NBDG [48, 49] and TMRE [50, 51] in tumor models. We have extensively validated the capability to image 2-NBDG and TMRE uptake in cells *in vitro* and *in vivo* using a murine window chamber model [48, 49, 51]. Further we have demonstrated that 2-NBDG, TMRE, and SO_2 imaging differentiates the adaptive phenotype of metastatic tumors from non-metastatic breast tumors [51] and used this as the foundation to develop an innovative strategy to measure 2-NBDG and TMRE simultaneously using intravital microscopy [50]. To translate simultaneous quantification of key metabolic endpoints to solid tumor models that are often used for therapeutic studies [52], we have developed a Monte Carlo (MC) algorithm, which when used with spectroscopy measurements of reflectance and fluorescence, quantifies tissue [Hb], SO_2, scattering [53, 54], and turbidity-free 2-NBDG and TMRE fluorescence [44, 55, 56].

In this study, we demonstrate near-simultaneous optical spectroscopy and MC modeling [44, 55, 56] to quantify vascular SO_2 and [Hb] along with 2-NBDG and TMRE uptake of a flank tumor model *in vivo*. We were able to adopt the sequential injection strategy previously developed for intravital microscopy to perform near-simultaneous quantification of glucose uptake and mitochondrial membrane potential *in vivo*. We observed that 4T1 tumors had a significant increase in 2-NBDG uptake, TMRE uptake and [Hb], but decreased SO_2 and scattering, compared to normal flank tissues. We also demonstrate that glucose uptake and oxidative phosphorylation quantified from spectroscopy were concordant with our formerly reported microcopy results [50]. Although 4T1 tumors have been considered as primarily glycolytic in the past [16, 22], our results demonstrate that it also relies on mitochondrial metabolism. A strong correlation was also observed between the metabolic (2-NBDG and TMRE) and vascular endpoints (SO_2 and [Hb]) in 4T1 tumors. None of these correlations were observed in normal tissue. The correlation studies suggest a strong coupling between substrate availability and demand in 4T1 tumors, but not in quiescent normal tissue. Quantitative optical spectroscopy is an effective tool for near-simultaneous *in vivo* quantification of vascularity and the major axes of metabolism in cancer, which is important for studying the mechanisms underlying cancer progression, metastasis, and resistance to therapies. Our technology will be able to seamlessly connect insights from *in vitro* studies to those from whole animal or patient imaging through local tissue measurements *in vivo.*

2. Materials and methods

2.1 Flank tumor model

All *in vivo* experiments described here were performed according to a protocol approved by Duke University Institutional Animal Care and Use Committee (IACUC). Female athymic nude mice (nu/nu, NCI, Frederick, Maryland) aged 8 to 10 weeks were used for these studies. All animals were housed in an on-site housing facility with ad libitum access to food and water and standard 12-hour light/dark cycles. A non-tumor animal study was used to further evaluate the sequential injection protocol for near-simultaneous optical spectroscopy of 2-NBDG and TMRE in a flank tumor model. A total of 20 non-tumor animals were randomly assigned to (1) TMRE only group (N = 6, 100 µL dose of 75 µM); (2) 2-NBDG only group (N = 7, 100 µL dose of 6 mM); and (3) TMRE→2-NBDG with 20-minute delay group (N = 7), the amounts and concentrations of TMRE and 2-NBDG used in the sequential injection group were exactly same as those used in the 2-NBDG only or TMRE only groups. Mice were fasted for 6 hours before optical spectroscopy to minimize variance in metabolic demand [48]. A separate group of tumor animal study (N = 9) was performed to demonstrate the usability of our protocol in solid tumors. These mice received a subcutaneous injection of 4T1 cells (0.1 mL of cell solution with a concentration of 10^6 cells/mL) in the right flank under isoflurane anesthesia. The mice were returned to the cage and monitored continuously for two weeks after the tumor cell injection. On day 10 after the tumor injection (tumor size is ~6 mm in diameter), mice were fasted for 6 hours and anesthetized with isoflurane for the

Biomedical Optics EXPRESS

spectroscopy study. All tumor animals received injection protocol (3) TMRE→2-NBDG with 20-minutes delay (100 µL dose of 75 µM TMRE→100 µL dose of 6 mM 2-NBDG).

2.2 Optical measurements

The optical spectroscopy system and fiber-probe were described in detail previously [44]. The optical measurement system is briefly illustrated in Fig. 1(A). The fiber-optics probe (Fig. 1(B)) consisted of 19 fibers for illumination and 18 surrounding fibers for detection. The numerical apertures of illumination fibers and detection fibers were all 0.22. The core diameters of the illumination and detection fibers were 200 µm. The sensing depth of the probe was estimated to be 1.5 mm from tissue-mimicking phantom studies. To count the lamp throughput change with time, all diffuse reflectance and fluorescence spectra on each set of experiments were calibrated using a diffuse reflectance standard (20%, Spectralon, Labsphere) and a fluorescence standard (USF 210-010, LabSphere), respectively. To further correct fluorescence spectra for wavelength response, the fluorescence spectra were further calibrated by a NIST-approved tungsten calibration lamp (Optronic Laboratories Inc.). All the optical measurements were performed on animals under anesthesia using a mixture of isoflurane and room air (1.5% v/v), and a heating pad was used to help mice maintain body temperature. Optical measurements on normal and tumor-bearing mice were obtained by placing the fiber probe gently on the flank (Fig. 1(C)) with the help of a custom designed probe holder (Fig. 1(B)). Diffuse reflectance spectra were acquired from 400 nm to 650 nm (integration time: 3.8 ms). Fluorescence emission spectra were acquired from 520 nm to 600 nm (integration time: 2 s) using excitation at 488 nm and from 565 nm to 650 nm (integration time: 5 s) using excitation at 555 nm. The 488 nm light was typically used for 2-NBDG excitation, while the 555 nm light was used for TMRE excitation. As reported previously, the use of these two light sources will result in negligible optical cross-talk between the fluorescence channels when biologically relevant concentrated TMRE (75 µM of 100 µL) and 2-NBDG (6 mM of 100 µL) were used [50]. All measurements were acquired in a dark room to minimize background noise. Prior to any injection, baseline diffuse reflectance and background fluorescence spectra (excited by 488 nm and 555 nm respectively) were measured from the tissue region of interest. After the injection, optical measurements on each mouse were acquired continuously for a period of 80 minutes (TMRE only group or TMRE→2-NBDG with 20-minute delay group) or 60 minutes (2-NBDG only group). Each animal was euthanized after the completion of all optical measurements based on the IACUC protocol. After optical measurements on each animal were complete, reference spectra on a diffuse reflectance standard (20%, Spectralon, Labsphere) and a fluorescence standard (USF 210-010, LabSphere) were measured for future calibration.

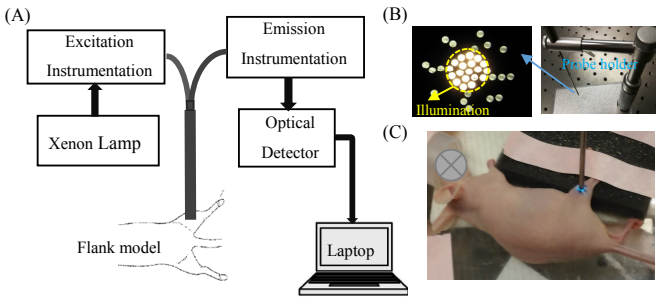

Fig. 1. (A) Schematic of the optical measurement setup; (B) Fiber-optics probe and custom designed probe holder; (C) Photo of a typical normal flank under optical measurement. The measurement site was marked by surgical pen.

Biomedical Optics EXPRESS

2.3 Calculation of vascular and metabolic parameters

In order to compare fluorescence intensities between tumor and normal tissue, it is essential to correct the tissue absorption and scattering induced distortions of the measured fluorescence signal. Both diffuse reflectance and fluorescence spectra across the wavelength range 500 nm to 650 nm are needed to remove absorption and scattering distortions on fluorescence using an inverse MC model. Our previously developed scalable inverse MC model [44] was used to extract tissue scattering, absorption, native fluorescence of 2-NBDG, and native fluorescence of TMRE from *in vivo* optically measured spectra. The reflectance and fluorescence-based inversion MC model has been decried in detail previously [44, 55, 56]. Generally, the MC model assumes oxygenated hemoglobin, deoxygenated hemoglobin, and overlying mice skin as absorbers while cells and cellular components as scatterers. The tissue absorption coefficient is calculated by utilizing the widely used extinction coefficients reported by Scott Prahl [57], and the tissue scattering is calculated using Mie theory for spherical particles [58]. The MC inverse model adaptively fits the modeled diffuse reflectance to the measured tissue reflectance until the sum of squares error between the modeled and measured diffuse reflectance is minimized. Since the MC model works on an absolute scale while the tissue measurements are relative to a reflectance standard, a reference phantom with known optical properties is created to scale the tissue optical properties accurately [44]. The MC fluorescence model assumes that the measured fluorescence is a function of fluorophore concentration, absorbed energy probability and fluorescence escape probability [55]. The absorbed energy probability and fluorescence escape probability rely on optical properties at excitation wavelength and emission wavelength respectively [55], thus they can be easily simulated once the absorption and scattering information is extracted to quantify intrinsic fluorescence. The extracted absorption spectra between 520 nm and 600 nm were used to estimate SO_2 and total hemoglobin concentration. The extracted intrinsic 2-NBDG and TMRE fluorescence spectra were used to estimate the glucose uptake and MMP. Specifically, the mean of the peak-band (emission peak wavelength ± 10 nm) fluorescence intensity of intrinsic 2-NBDG and TMRE spectra were used to represent the 2-NBDG and TMRE signal. The 2-NBDG and TMRE signals taken at different time points were used to create the kinetic uptake curves. Comparison of mean kinetic curves across animal groups was performed using a two-way analysis of variance (ANOVA) test followed by Tukey-Kramer post-hoc tests. The fluorescence intensities, [Hb], SO_2, or average scattering among different groups were compared with a two-sample t-test. A p-value < 0.05 was considered to be statistically different among the two groups under comparison.

3. Results

3.1 Sequential injection of TMRE and 2-NBDG enables near-simultaneous measurement of glucose uptake and MMP in a flank model

Our former study [50] has demonstrated that there is neither significant optical cross-talk in tissue mimicking phantoms nor chemical crosstalk by mass spectrometry analysis between 2-NBDG and TMRE, suggesting that they are suitable for combined fluorescence imaging. However our *in vivo* non-tumor window chamber study showed that there was strong biological cross-talk when we injected the two probes at the same time. Specifically, TMRE signal was significantly attenuated by 2-NBDG when the two probes were injected simultaneously. We established that injecting TMRE first and then 2-NBDG after a 10-20 minute delay results in negligible crosstalk during simultaneous imaging of TMRE and 2-NBDG in a non-tumor window chamber model. Here we wanted to further establish that our previously validated sequential injection strategy [50] is applicable for quantitative optical spectroscopy of turbidity corrected TMRE and 2-NBDG fluorescence in a flank tumor model. Towards this goal, we compared turbidity-corrected fluorescence spectra measured from mice receiving injections of either 2-NBDG alone, TMRE alone, or TMRE followed by 2-NBDG

Biomedical Optics EXPRESS

with a 20-minute delay. Mice were monitored using optical spectroscopy for 60 minutes (2-NBDG alone) or 80-minutes (TMRE alone or sequential injection) post administration of the fluorescent indicators.

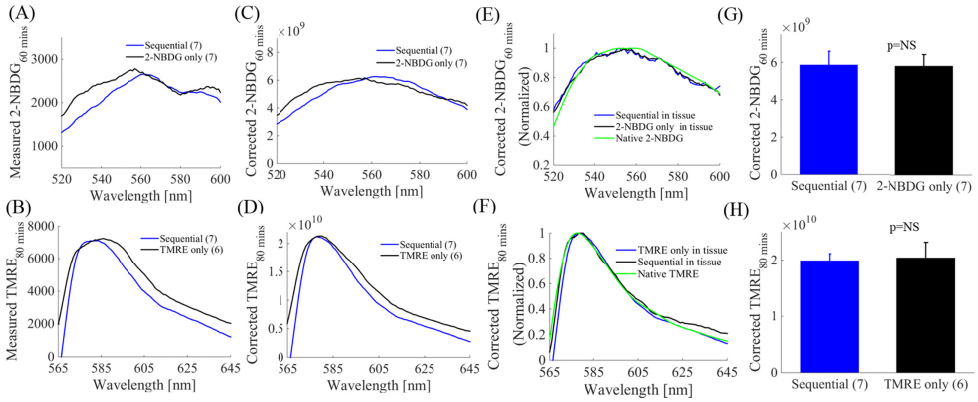

Fig. 2. When a staggered delivery scheme was used, 2-NBDG and TMRE fluorescence closely recapitulated the results that were obtained when 2-NBDG or TMRE was administered alone in a flank model. Optical spectroscopy was performed on normal flanks after they received one of the three distinct injection strategies: 1) 2-NBDG alone (100 µL dose of 6 mM); 2) TMRE alone (100 µL dose of 75 µM), 3) Sequential injection: TMRE (100 µL dose of 75 µM) followed by 2-NBDG (100 µL dose of 6 mM) with a 20-minute delay. Notes that there was 20-minute delay between TMRE injection and 2-NBDG injection, thus the 2-NBDG_{60} and $TMRE_{80}$ uptake were actually measured at the same time point. (A) Representative measured 2-NBDG_{60} spectra from normal tissue were distorted by hemoglobin concentration. (B) Representative measured $TMRE_{80}$ spectra from normal flanks were distorted by tissue background. (C) Correction with the MC fluorescence model removed hemoglobin-induced distortions on 2-NBDG fluorescence. (D) Correction with the MC fluorescence model removed tissue background-induced distortions on TMRE fluorescence. (E) MC corrected 2-NBDG_{60} spectra from normal tissue, normalized to their respective maxima are presented along with a true 2-NBDG fluorescence measurement, illustrating good agreement between the extracted *in vivo* spectral line shapes and native 2-NBDG. (F) MC model corrected $TMRE_{80}$ spectra from normal tissue, normalized to their respective maxima are presented along with a true TMRE fluorescence measurement, illustrating good agreement between the extracted *in vivo* spectral line shapes and native TMRE. (G) MC model corrected 2-NBDG_{60} uptake in normal tissue are not statistically different among the sequential injection group and 2-NBDG only group. (H) MC corrected $TMRE_{80}$ uptake in normal tissue are not statistically different among the sequential injection group and TMRE only group. NS = not significant. N = 6-7 mice/group. Error bars in the graphs represent standard error. Comparison of the mean intensity of $TMRE_{80}$ or 2-NBDG_{60} across animal groups was performed with two sample t-tests using the MATLAB (Mathworks, USA) statistics toolbox.

Fig. 2(A) and 2(B) show representative raw 2-NBDG and TMRE fluorescence spectra, respectively measured on normal flanks. The spectra in blue were measured on animals that received sequential injection of TMRE followed by 2-NBDG, while the spectra in black were measured on animals that received either 2-NBDG or TMRE injection only. The shape of the spectra shows visible distortion, which is likely caused by tissue hemoglobin absorption [44]. We applied our previously developed scalable MC reflectance and fluorescence models [44, 55, 56] to the measured fluorescence spectra and these distortions were removed effectively as shown in Fig. 2(C) and 2(D). The normalized 2-NBDG fluorescence spectra and TMRE fluorescence spectra after MC model correction along with their native spectra (green) in Fig. 2(E) and 2(F) show that the shape of the recovered spectra match well with the actual 2-NBDG and TMRE spectra. Figure 2(G) shows that 2-NBDG uptake at 60-minutes post-injection is comparable between the sequential injection and 2-NBDG only injection groups. Similarly, Fig. 2(H) demonstrates that the TMRE uptake 80-minute post injection obtained from the sequential injection group is statistically similar to the TMRE injection only group.

Biomedical Optics EXPRESS

The excellent match between the MC corrected fluorescence spectra and native fluorescence spectra for both 2-NBDG and TMRE further confirms the effectiveness of the sequential injection strategy [50, 56]. In the rest of manuscript, all reported TMRE and 2-NBDG data was MC fluorescence model corrected.

3.2 Optical measurements of intrinsic 2-NBDG and TMRE fluorescence demonstrate increased glucose uptake and increased mitochondrial metabolism in 4T1 solid murine breast tumors compared with normal tissue

We investigated glucose uptake and mitochondrial membrane potential of a metastatic solid tumor line (4T1) by comparing uptake and washout kinetic curves of 2-NBDG and TMRE fluorescence. Figure 3(A) and 3(B) show representative intrinsic 2-NBDG$_{60}$ (2-NBDG fluorescence at 60 minutes post 2-NBDG injection) and TMRE$_{80}$ (TMRE fluorescence at 80 minutes post TMRE injection) fluorescence spectra measured on normal tissue and 4T1 tumors. The average 2-NBDG$_{60}$ and TMRE$_{80}$ spectra are significantly higher in 4T1 tumors compared to that in normal tissue ($p<0.05$ and $p<0.001$ respectively). Figure 3(C) shows that 4T1 tumors have similar 2-NBDG kinetic profiles but different intensities compared to normal tissue. Figure 3(D) shows that the TMRE kinetic curves for tumors were significantly different compared to that in normal tissue ($p<0.01$). Figure 3(E) and 3(F) show 2-NBDG$_{60}$ uptake and TMRE$_{80}$ uptake in 4T1 tumors and normal tissue respectively. The average 2-NBDG$_{60}$ and TMRE$_{80}$ uptake in 4T1 tumors was significantly higher than that in normal tissue ($p<0.05$ and $p<0.001$ respectively). Increased glucose uptake and oxidative phosphorylation in 4T1 tumors captured by our spectroscopy system is consistent with our former microscopy studies [50, 51].

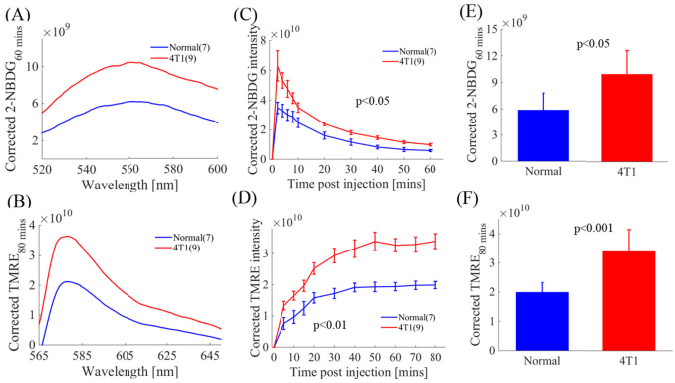

Fig. 3. Optical quantification of intrinsic 2-NBDG fluorescence and TMRE fluorescence from tissue captures increased glucose uptake and increased mitochondrial metabolism in metastatic solid tumors compared with normal tissue. (A) MC model corrected 2-NBDG$_{60}$ spectra from normal tissue and 4T1 tumors. (B) MC model corrected TMRE$_{80}$ spectra from normal tissue and 4T1 tumors. (C) Representative 2-NBDG kinetic profiles obtained from MC corrected 2-NBDG fluorescence for normal tissue and 4T1 tumors. (D) Representative TMRE kinetic profiles obtained from MC corrected TMRE fluorescence for normal tissue and 4T1 tumors. (E) MC corrected 2-NBDG$_{60}$ uptake is significantly higher in 4T1 tumors compared with normal tissue ($p<0.05$). (F) Corrected TMRE$_{80}$ is significantly higher in 4T1 tumors compared with normal tissue ($p<0.001$). NS = not significant. N = 7-9 mice/group. Error bars in the graph represent standard errors. Comparison of the mean intensity of 2-NBDG$_{60}$ and TMRE$_{80}$ across animal groups was performed with two sample t-tests using the MATLAB (Mathworks, USA) statistics toolbox. Comparison of mean kinetic curves across animal groups was performed with a two-way Analysis of Variance (ANOVA) test using the MATLAB (Mathworks, USA) statistics toolbox.

Biomedical Optics EXPRESS

3.3 Optical measurements of vascular endpoints demonstrate that 4T1 tumors have distinct vascular microenvironment compared to non-tumor tissue

The vascular microenvironment is a critical enabler of tumor survival and recurrence since it will influence tumor metabolism by affecting substrate availability directly. To investigate the tumor vascular microenvironment, we also quantified the wavelength dependent absorption coefficient (μ_a), reduced scattering coefficient (μ_s'), and derived SO_2 and [Hb] using Beer's law. Baseline SO_2 levels measured soon after the administration of isoflurane anesthesia but prior to the injection of the contrast agents was measured to avoid the confounding effects of either anesthesia or the contrast agents [59]. Figure 4(A) shows representative calibrated diffuse reflectance spectra from normal tissue and a 4T1 tumor. Open circles represent the measured spectra and the solid lines represent MC model fitted spectra. Figure 4(B) shows that the MC model extracted absorption coefficient spectrum is higher in 4T1 tumors compared to that in normal tissue. Figure 4(C) shows that the scattering coefficient spectrum is lower in 4T1 tumors compared to that in normal tissue. Baseline SO_2 levels and [Hb] were extracted from the absorption spectra. SO_2 was significantly lower in solid 4T1 tumors compared with normal tissue ($p<0.005$) (Fig. 4(D)), while baseline [Hb] was significantly higher in solid 4T1 tumors compared with normal tissue ($p<0.05$) (Fig. 4(E)). Figure 4(F) shows that average scattering levels are significantly lower in solid 4T1 tumors compared with normal tissue ($p<0.01$).

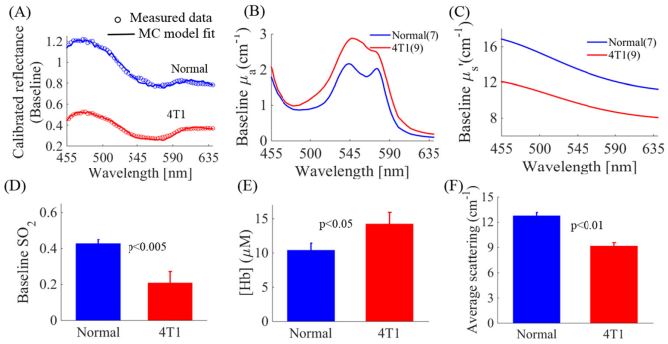

Fig. 4. Baseline SO_2 and average scattering levels are significantly lower, while baseline [Hb] are significantly higher in solid 4T1 tumors compared with normal tissue. (A) Representative measured reflectance spectra (open circles) and MC model fitted spectra (solid line) from normal tissue (blue) and 4T1 tumors (red). (B) Extracted absorption spectra illustrate higher absorption in 4T1 tumors compared with normal tissue. (C) Extracted scattering spectra illustrate lower scattering in 4T1 tumors compared with normal tissue. (D) Baseline SO_2 levels are significantly lower in 4T1 tumors compared with normal tissue ($p<0.005$). (E) Baseline hemoglobin concentrations are significantly higher in 4T1 tumors compared with normal tissue ($p<0.05$). (F) Average scattering levels are significantly lower in 4T1 tumors compared with normal tissue ($p<0.01$). NS = not significant. N = 7-9 mice/group. Error bars in the graph represent standard errors. Comparison of the mean baseline SO_2 across animal groups was performed with two sample t-tests using the MATLAB (Mathworks, USA) statistics toolbox.

3.4 Optical endpoints reveal a distinct relationship between metabolism and vasculature for metastatic solid tumors

Measurement of key vascular and metabolic endpoints on the same tissue site enables us to explore the interplay between metabolism and the vascular microenvironment. Figure 5 shows scatter plots of the relationship between different combinations of the four endpoints measured using optical spectroscopy (scattering was excluded). All of the 2-$NBDG_{60}$ and $TMRE_{80}$ values were normalized to the global highest value, i.e. the highest 2-$NBDG_{60}$ and $TMRE_{80}$ across all normal and tumor mice. The top panel of Fig. 5 shows the correlations among the metabolic and vascular endpoints for 4T1 tumors, while the bottom panel of Fig. 5 shows correlations for normal tissue. Figure 5(A) and 5(C) show that both 2-$NBDG_{60}$ (r =

Biomedical Optics EXPRESS

0.78, p = 0.01) and $TMRE_{80}$ (r = 0.64, p = 0.05) in 4T1 tumors are positively correlated with baseline SO_2 levels. In contrast, both 2-$NBDG_{60}$ (r = –0.51, p = 0.25) and $TMRE_{80}$ (r = –0.57, p = 0.18) are negatively correlated with baseline SO_2 levels in normal tissues as shown in Fig. 5(B) and 5(D), while the correlations are not statistically significant. It is interesting to note that 2-$NBDG_{60}$ and $TMRE_{80}$ are positively correlated with [Hb] for both 4T1 tumors (Fig. 5(E) and 5(G)) normal tissues (Fig. 5 (F) and (H)), though the correlations again are only significant for 4T1 tumors (2-$NBDG_{60}$ with [Hb]: r = 0.79, p = 0.01; $TMRE_{80}$ with [Hb]: r = 0.70, p = 0.03). Figure 5(I) shows that there is a strong positive correlation between 2-NBDG and TMRE uptake (r = 0.89, p = 0.001) in 4T1 tumors, while no obvious correlation between 2-NBDG and TMRE uptake is observed for normal tissue as shown in Fig. 5(J) (r = 0.24, p = 0.61). In summary, all of the pairwise correlations are significant for the 4T1 tumors while none of the correlations are significant for normal tissues.

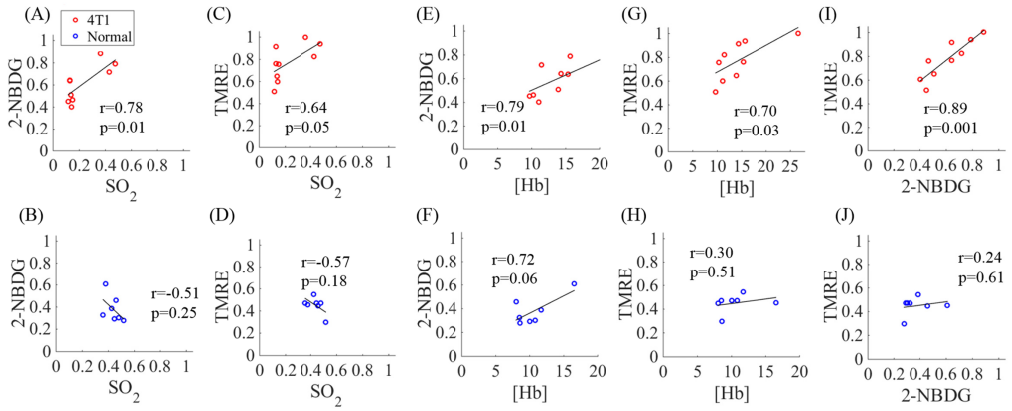

Fig. 5. Optical quantification of baseline SO_2, [Hb], final 2-NBDG uptake, and final TMRE uptake reflects different relationships between metabolism and vascular microenvironment in metastatic tumors (4T1) and normal tissue. Scatter plots show relationships of 2-$NBDG_{60}$ and baseline SO_2 for (A) 4T1 tumors and (B) normal tissue. Relationship of $TMRE_{80}$ and baseline SO_2 for (C) 4T1 tumors and (D) normal tissue. Scatter plots show relationships of 2-$NBDG_{60}$ and [Hb] for (E) 4T1 tumors and (F) normal tissue. Scatter plots show relationships of $TMRE_{80}$ and baseline [Hb] for (G) 4T1 tumors and (H) normal tissue. Scatter plots show relationships of 2-$NBDG_{60}$ and $TMRE_{80}$ for (I) 4T1 tumors and (J) normal tissue. Both 2-NBDG and TMRE values were normalized to the global highest value, i.e. the highest 2-NBDG and TMRE across all normal and tumor mice. The 2-NBDG and TMRE uptakes were measured at the same time point due to the delayed injection strategy.

4. Discussion

Quantifying metabolic endpoints in the context of tumor vasculature is of great interest to cancer biologists studying therapeutic efficacy. Toward our ultimate goal of a robust tool for near-simultaneous quantification of metabolism and vasculature in diverse cancer applications, our current work in 4T1 tumors and normal flanks serves to optimize and validate the optical spectroscopy system, the MC model and sequential injection protocol previously established with intravital microscopy for the quantitation of glucose uptake, mitochondrial membrane potential, oxygen saturation, hemoglobin concentration and scattering of solid tumors and normal tissues *in vivo*. Optical spectroscopy and imaging can also leverage endogenous contrast to provide quantitative endpoints related tumor metabolism. The two endogenous fluorophores in tissue, reduced nicotinamide adenine dinucleotide (NADH) and flavin adenine dinucleotide (FAD) [43, 45] have provided insights into the reduction-oxidation state in the electron transport chain, since higher NADH fluorescence corresponds to tumors that rely more on glycolysis while increased FAD fluorescence corresponds to more oxidative tumors [46]. Our strategy to use 2-NBDG and

Biomedical Optics EXPRESS

TMRE complements these endogenous fluorescence imaging approaches in that it reports on metabolic endpoints that are related to but distinct from the redox ratio endpoints.

We have previously demonstrated near-simultaneous imaging of glucose uptake, mitochondrial membrane potential of tumors in dorsal window chamber models using intravital microscopy [50]. Our former study confirmed that there is neither significant optical cross-talk in phantoms nor chemical cross-talk in mass spectrometry samples between 2-NBDG and TMRE [50], suggesting that they are suitable for combined fluorescence imaging when injected in a staggered manner (TMRE followed by 2-NBDG after a 10-20 minute delay) into the animal model. In this study, we further confirmed the effectiveness of the sequential injection strategy for near-simultaneous optical spectroscopy of 2-NBDG and TMRE uptake in a flank tumor model. The consistency in the data obtained with the spectroscopy system and our formerly reported microscopy systems demonstrates the robustness of our technique for near-simultaneous measurement of glucose uptake and mitochondrial membrane potential. Dorsal window chambers are by design optically thin and therefore provide an excellent model system to image small tumors with an intact tissue microenvironment via microscopy, however the dorsal window chamber cannot be imaged longitudinally beyond a few weeks, which limits its application to short-term *in vivo* studies [60]. In contrast, solid tumor models are particularly well-suited for long-term *in vivo* studies using optical spectroscopy such as monitoring tumor growth and assessing response to treatment [61], thus it is most often used for therapeutic studies [52].

Using our method, we were able to recapitulate known metabolic phenotypes in normal tissue and tumors. We demonstrated that 4T1 tumors have high mitochondrial activity in addition to glycolysis. The increased mitochondrial metabolism and glycolysis in 4T1 tumors compared to the normal flank recapitulated the results from our previous intravital microscopy studies [50, 51]. The increased 2-NBDG uptake in 4T1 tumors also matched well with published reports including a Seahorse Assay study [2], magnetic resonance spectroscopy studies [2, 62], metabolomics study [63], and FDG-PET study [62], all suggesting that 4T1 tumors have increased glucose uptake compared to normal tissue. It is interesting to note that the 4T1 tumors also have high mitochondrial activity in addition to glycolysis [5], which is consistent with the results published previously [16]. Specifically, Simões et al [16] utilized both magnetic resonance spectroscopy and the Seahorse Assay to characterize the tumor metabolism in which they captured both increased glycolysis and increased oxidative phosphorylation activity in 4T1 tumors compared to its sibling non-metastatic tumor lines. Several studies showed that 4T1 tumors, which are highly metastatic and aggressive, are likely more “adaptable” to micro-environmental changes [16, 22, 64]. These “adaptable” tumors have the capacity to rely on both glycolytic and mitochondrial metabolism under a range of oxygen conditions allowing them to survive therapeutic stress, promoting negative outcomes such as increased recurrence [65], migration [66] and metastatic propensity [67].

The absorption and scattering properties for both normal flanks and small solid 4T1 flank tumors measured by our quantitative optical spectroscopy system are consistent with published reports [68, 69]. We observed that 4T1 tumors have higher absorption and lower scattering coefficients compared to normal tissues. The increased absorption in 4T1 tumors is likely caused by angiogenesis [44, 70, 71] as evidenced by the increased hemoglobin concentration in tumors. In fact, angiogenesis induced by 4T1 tumor cells begins at a very early stage [72], i.e., when the tumor mass contains roughly 100-300 tumor cells. Moreover, 4T1 tumors were found to have robust HIF-1a and VEGF levels [73] that could promote angiogenesis and hypoxia. Our spectroscopy study showed that solid flank 4T1 tumors had significantly lower baseline SO_2 values compared to normal tissues, suggesting that these solid flank tumors likely have regions of hypoxia [74, 75]. It is worth mentioning that our former microscopy study found that the baseline SO_2 values were comparable between normal tissue and 4T1 tumors in window chamber models [51]. This difference in the

Biomedical Optics EXPRESS

baseline SO_2 values of 4T1 tumors in window chambers and flanks suggests that the baseline SO_2 levels in tumors are related to tumor size; small 4T1 tumors in window chambers (~2 mm in diameter) have higher oxygenation values while the larger 4T1 tumors in flank tumors (~6 mm in diameter) are more likely to be hypoxic. Hypoxia plays an important role in tumor cells that evade traditional therapies [76–78]. Our non-invasive optical quantification of vascular endpoints in animals offers an opportunity to study the tumor microenvironment and its effect on tumor metabolism.

We also demonstrated that the metabolic endpoints are positively correlated with their corresponding vascular endpoints for 4T1 tumors but not for normal tissue. Moreover, optical spectroscopy of key metabolic endpoints reveals a strong positive correlation between 2-NBDG and TMRE uptake in 4T1 tumors but not in normal tissue. We did not observe correlations between metabolic endpoints and baseline SO_2 values for normal animals which is likely attributed to the high baseline SO_2 values seen in normal tissue. In contrast, there was considerable variance in vascular endpoints for the solid 4T1 tumors which is likely due to the fact that tumor hypoxia is unstable both spatially and temporally [79]. The positive correlations between metabolic and vascular endpoints suggest that 4T1 tumors highly rely on substrate availability [16].

5. Conclusion

Our preclinical study demonstrates that optical spectroscopy is an effective tool for simultaneously quantifying vascularity and metabolism of cancer, which is critical to understand mechanisms underlying cancer progression, metastasis and resistance to therapies. Quantitation of tumor mitochondrial membrane potential and glucose uptake could provide insight into how metabolism modulates therapeutic outcomes and tumor cell survival following therapy. The associated tumor vasculature within the tumor microenvironment also influences tumor metabolism and being able to quantify both energy supply and demand will provide a holistic view of tumor bioenergetics. Quantitative optical spectroscopy enables longitudinal *in vivo* studies, at a length scale that complements existing methods, and thus has the potential to facilitate novel inter-disciplinary studies in cancer pharmacology.

Funding

NIH (5R42CA156901-03).

Acknowledgements

The funders had no role in study design, data collection and analysis, decision to publish, or preparation of the manuscript.

Disclosures

Dr. Ramanujam has founded a company called Zenalux Biomedical and she and other team members have developed technologies related to this work where the investigators or Duke may benefit financially if this system is sold commercially.